Statistical studies on Mars atmospheric sputtering by precipitating pickup O+: Preparation for the MAVEN mission

Yung-Ching Wang, Janet G. Luhmann, Xiaohua Fang, François Leblanc, Robert E. Johnson, Yingjuan Ma, Wing-Huen Ip

AGU PUBLICATIONS

JGR

Journal of Geophysical Research: Planets

RESEARCH ARTICLE

10.1002/2014JE004660

Key Points:
- Sputtering loss rates are controlled by the environments
- Solar wind is the major driver to determine the pickup ion sputtering
- Sputtering response relations are derived for the preparation of MAVEN mission

Correspondence to:
Y.-C. Wang,
ychwang@must.edu.mo

Citation:
Wang, Y.-C., J. G. Luhmann, X. Fang, F. Leblanc, R. E. Johnson, Y. Ma, and W.-H. Ip (2015), Statistical studies on Mars atmospheric sputtering by precipitating pickup O^+: Preparation for the MAVEN mission, *J. Geophys. Res. Planets*, *120*, 34–50, doi:10.1002/2014JE004660.

Received 5 MAY 2014
Accepted 14 OCT 2014
Accepted article online 21 OCT 2014
Published online 23 JAN 2015

Statistical studies on Mars atmospheric sputtering by precipitating pickup O^+: Preparation for the MAVEN mission

Yung-Ching Wang[1,2], Janet G. Luhmann[1], Xiaohua Fang[3], François Leblanc[4], Robert E. Johnson[5], Yingjuan Ma[6], and Wing-Huen Ip[2,7]

[1]Space Sciences Laboratory, University of California, Berkeley, California, USA, [2]Space Science Institute, Macau University of Science and Technology, Macau, China, [3]Laboratory for Atmospheric and Space Physics, University of Colorado Boulder, Boulder, Colorado, USA, [4]LATMOS/IPSL-CNRS, Université Pierre et Marie Curie, Paris, France, [5]Department of Engineering Physics, University of Virginia, Charlottesville, Virginia, USA, [6]Institute of Geophysics and Planetary Physics, University of California, Los Angeles, California, USA, [7]Institutes of Astronomy and Space Science, National Central University, Jhongli, Taiwan

Abstract With the upcoming MAVEN mission, the role of escape in the evolution of the Martian atmosphere is investigated in more detail. This work builds on our previous modeling of the atmospheric impact of the pickup O^+ sputtering effects for various solar wind parameters, solar EUV intensities, and the surface crustal field distributions. Relationships between the incident ion properties and the ejected hot neutral components, often referred to as atmospheric sputtering, are derived for application to proposed MAVEN ion spectrometer measurements of precipitating O^+. We show how our simulation results can be used to constrain the sputtering effects under present conditions and to interpolate toward estimates of sputtering efficiencies occurring in earlier epochs. Present-day sputtering under typical circumstance is estimated to be weak but possibly detectable as an exospheric enhancement. The ultimate goal of estimating the importance of atmospheric sputtering effects on the evolution of the Martian atmosphere can be better deduced by the combining MAVEN measurements with models and the sputtering response relations derived here.

1. Introduction

Although there is considerable evidence for water having been on the surface, the major outstanding question is how it was and when it was lost. The evolution of the atmosphere plays an important role in the determination of the fate of the possible early liquid water [*Jakosky and Jones*, 1997; *Carr*, 1999; *Zuber et al.*, 2000; *Chassefière and Leblanc*, 2004; *Lammer et al.*, 2013]. From geomorphological analysis, water oceans with depth of around 150 m could have been present on the surface under much thicker atmosphere and warmer climate conditions than today [*Chassefière and Leblanc*, 2004]. After the disappearance of the Mars intrinsic dipole fields, around 700 Myr after the planet's origin, a significant fraction of the atmosphere could have been removed by escape to space in the absence of the protection by strong magnetic fields [*Acuña et al.*, 1998; *Chassefière and Leblanc*, 2004]. Simultaneously, the primitive water elements could have been lost to space by the escape of H and O atoms or ions dissociated from H_2O. Therefore, a key issue is to understand Martian atmospheric loss mechanisms at the present time in order to estimate escape rates in earlier epochs and their relevance to a possible ancient water ocean.

As the major objective of the Mars Atmosphere and Volatile Evolution (MAVEN) mission, the Martian atmospheric structure and its evolutions can be better constrained after Mars Orbital Insertion on 22 September 2014. With the instruments on board, the pickup ion density and speeds, the composition of atmospheric neutrals and ions, UV emission profiles, and controlling factors including solar wind parameters and solar EUV flux can be measured simultaneously in the Martian exosphere and upper atmosphere. The volatiles loss rates can therefore be analyzed with the goal of evaluating the various proposed mechanisms, including thermal escape, ion outflow, photochemical-induced escape, and atmospheric sputtering. While thermal escape is important for lighter elements such as H and He, other loss processes compete for significance for heavier species such as O. Among these, pickup ion sputtering effects could have a nonnegligible influence which can vary with solar wind pressure, interplanetary magnetic fields (IMF), and solar EUV intensity,

as well as the positions of the surface crustal fields and the tilting of the rotational axis due to the diurnal and seasonal variations of Mars.

When the newly formed ions, mainly O^+ ions, from the exosphere are picked up by the solar wind flow and IMF and transported downstream, a portion of the ions can reimpact the upper atmosphere and induce collision cascades with the neutrals. The associated sputtering process caused by the incidence of these energetic particles can produce higher-energy neutrals that create a hot corona above the exobase. Some of the sputtered particles can even gain enough energy to overcome Mars gravity and escape to the space. The first estimate of the pickup ion sputtering on Mars and Venus came from the study of *Luhmann and Kozyra* [1991]. Later, *Luhmann et al.* [1992] concluded that although the escape of elements due to sputtering may not be the major loss mechanism under present nominal solar conditions, its effects may have been much larger in earlier epochs and could even have become dominant. Under the same assumptions of different increments of solar EUV intensity to represent the environments at different epochs, further studies using improved atmospheric models also provided comparable results [*Johnson and Luhmann*, 1998; *Leblanc and Johnson*, 2001, 2002]. Combining a hybrid model, hot corona calculations, and sputtering simulations, *Chaufray et al.* [2007] also deduced that the sputtered hot corona and escape rates of O are currently smaller than those from the dominant dissociative recombination of O_2^+ under normal solar wind interactions. Recent studies that included enhanced solar wind, such as the passing of interplanetary coronal mass ejections (ICMEs), solar energetic particle event, or corotating interaction regions (CIRs), suggested that the sputtering effects may significantly increase for short periods due to vary large transient ion precipitation fluxes and energies [*Leblanc et al.*, 2002; *Hara et al.*, 2011; *Wang et al.*, 2014]. On the other hand, the existence of the surface crustal fields and their various interactions with the IMF can affect the pickup ion escape rates and the precipitation energy and fluxes as well as the resulting sputtering efficiencies [*Ma et al.*, 2004; *Ma and Nagy*, 2007; *Fang et al.*, 2010; *Li et al.*, 2011]. Therefore, an overview of sputtering effects covering a range of Mars environments and related interaction with the solar wind should be studied in more detail to get better estimates of the variability of these effects and their influence on Martian atmosphere evolution.

To derive the sputtering effects from the reimpact of the pickup O^+ on the neutral upper atmosphere, models for the solar wind interaction, pickup ion transport, and the neutral atmosphere collisional cascade calculations are needed. Since each of these individual model has been described and their results published, detailed information can be found in previous papers [*Ma et al.*, 2004; *Leblanc and Johnson*, 2002; *Fang et al.*, 2008; *Wang et al.*, 2014]. We thus provide only a short introduction to each of the model and their specific features in section 2. Simulation results for the pickup O^+ precipitations and the related sputtering effects are summarized for comparisons of six case studies in section 3. Toward the preparation for the MAVEN mission, we also develop an analysis tool for the quick estimation of sputtering effects based on expected O^+ precipitation measurements. The sputtering response relations between the modeled incident pickup O^+ fluxes and the resultant sputtered components derived from the six cases in our study are shown in section 4. Further improvements to be achieved and the applications of the sputtering response relations to measurements are discussed in more detail in section 5.

2. Simulation Models

The 3-D nonideal, multispecies, single-fluid MHD model based on the BATS-R-OS code is used to simulate, to the first order, the solar wind interaction with Mars [*Ma et al.*, 2004; *Ma and Nagy*, 2007]. In the model, the surface crustal field distributions are adopted from the *Arkani-Hamed* [2001] with 60° harmonic expansion. Detail on the photochemical reactions in the model, including solar EUV photoionization and charge exchange in the atmosphere and the ionosphere above an inner boundary of 100 km, can be found in *Ma et al.* [2004]. With its spherical grid structure, the influences of the ionosphere and the crustal field can be analyzed with high resolutions at lower altitudes.

Because the MHD model cannot provide pickup ion distribution functions, including their energy and angular spectra and kinetic trajectory effects, which are important to determine the sputtering process when they precipitate back into the upper atmosphere, an additional test particle simulation is used based on the field and flow parameters from the MHD model [*Fang et al.*, 2008]. The plasma density, velocity, and the electron temperature are utilized to calculate the pickup O^+ production rates. Three ionization mechanisms including photoionization, charge exchange, and electron impact are introduced [*Cravens et al.*, 1987; *Ma et al.*, 2004; *Fang et al.*, 2008]. With the parallelized 3-D Monte Carlo model applied here, billions of test

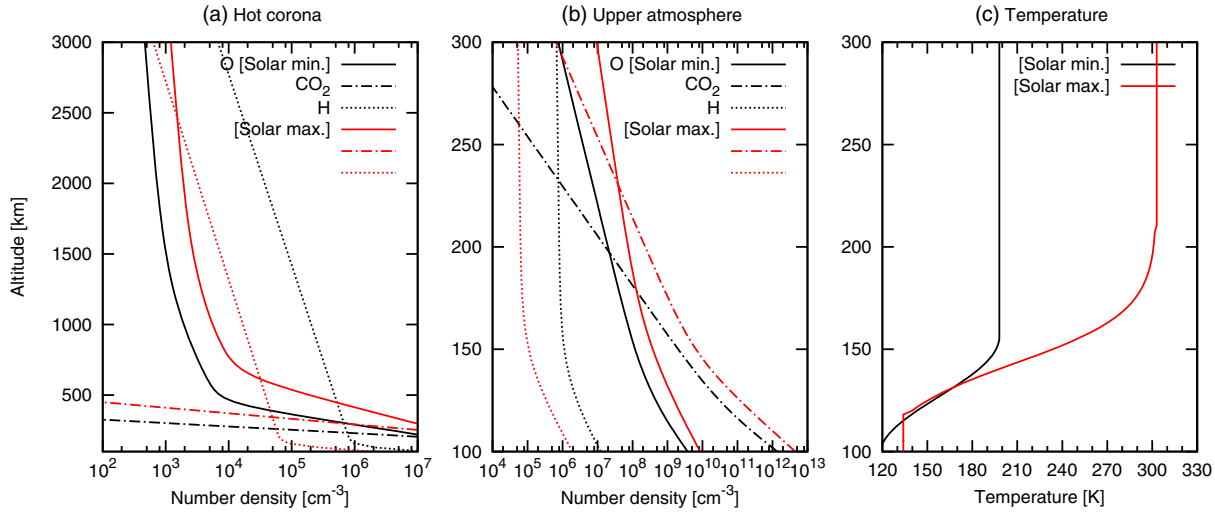

Figure 1. The initial atmosphere structure applied in the models. (a and b) The higher and lower altitude distributions of the number densities of O, CO_2, H, and (c) the temperature distribution of the upper atmosphere. Both initial atmospheres for the solar maximum and minimum cases are shown for comparisons.

particles can be traced to reconstruct realistic pickup O^+ precipitation distributions, with their spatial, energy, and angular information preserved in a large array. The background electromagnetic fields around Mars from the MHD simulation, combined with the test particle code, produce the well-established asymmetry signatures in the pickup ion spatial distribution and trajectories due to the acceleration of the pickup ions by the solar wind convection electric field. This combination can produce many of the features seen in hybrid models and pickup ion observations [*Brain et al.*, 2010, and reference therein]. One of the advantages in this case is the high spatial resolution description of the fields provided by the MHD code, although the drawback is in self-consistency, in that the larger gyroradius ions' effects on the MHD fluid are not included.

With the precipitation distributions from the pickup ion transport simulation results in hand, we can apply them as the input sources in the atmospheric sputtering model. For this purpose, we define an inner boundary at an altitude near the normal exobase where we both cease to create a source of pickup ions and also record what passes through it as precipitation. Therefore, the precipitated pickup O^+ collected from the ion test particle simulation can be traced continuously within the sputtering model. We assume that the ions are immediately neutralized by charge exchange [*Luhmann and Kozyra*, 1991] and trace them as neutrals after crossing the boundary. However, the treatment of this boundary is a challenging issue since there is no such exact division between collisional and collisionless regimes in the natural system, and charge exchange processes may occur at different altitudes related to different ion energies and scale heights of the atmosphere. Fortunately, the magnitude of the electric fields are normally small enough at lower altitudes, and the pickup ions should collide with the upper atmospheric neutrals before the acceleration effects from the electromagnetic fields become significant enough to influence their paths below the chosen boundary. The initial atmospheric density and temperature distributions in MHD, pickup ion transport, and atmospheric sputtering models for cases with different solar EUV intensities are shown in Figure 1 [*Ma et al.*, 2004, and references therein]. We have set the boundaries between the collisionless and collisional domain at 300 and 200 km at solar maximum and minimum, respectively. At the present time, we use spherically symmetric atmospheres to study the precipitation of the pickup O^+. In this way, we can identify the ion impact distributions corresponding to their production distributions and transport, regardless of the influences from the initial atmosphere structures corresponding to different longitudes and latitudes. The effects from more realistic 3-D atmosphere and exosphere structure and the resultant pickup ion precipitations will be investigated in the future.

Although different descriptions of the initial atmospheres may influence the solar wind interactions and the pickup ion precipitation distributions, their impact on the sputtering processes is limited when the same incident ion precipitates on different atmospheres as long as the major component near the exobase region is CO_2 [*Wang et al.*, 2014]. The 1-D atmospheric sputtering model is developed by *Leblanc and Johnson* [2002] and is extended to 3-D by *Wang et al.* [2014]. Detailed explanations on the calculations of

Table 1. The Settings of Conditions of the Simulated Cases

Cases	n_{sw} (cm^{-3})	V_{sw} (km/s)	IMF (nT)	Crustal Fields	Solar Cycle
Quiet	4	400	3 (Parker spiral toward Mars)	noon	max.
Active	4	1200	3 (B_y only, toward dusk)	noon	max.
Extreme	20	1000	20 (B_y only, toward dusk)	noon	max.
NoonC	4	400	3 (Parker spiral toward Mars)	noon	min.
DawnC	4	400	3 (Parker spiral toward Mars)	dawn	min.
NoC	4	400	3 (Parker spiral toward Mars)	not included	min.

the collisions including the impact parameters and interaction potential can be found in *Johnson and Liu* [1998], *Johnson et al.* [2000], *Leblanc and Johnson* [2002], and *Wang et al.* [2014]. The collisional frequency F_c are determined within the collisional domain above an lower boundary of 105 km as [*Bird*, 1994]

$$F_c = \frac{1}{2} n_f n_{th} \sigma_T |V_f - V_{th}| \quad (1)$$

where n_f, n_{th}, V_f, and V_{th} are the number densities and velocities of the energetic and thermal particles, respectively, and σ_T is the collisional cross section between them. Initially, the energetic particles are all incident pickup ions. As collisions occur and energy transformations take place, some of the original thermal neutrals will gain energies and become part of the energetic particles. The collisional processes will be calculated until a quasi steady state is reached. All of the energetic particles will be traced simultaneously at each time step within the collisional and the collisionless domain below $3R_M$ from the center of Mars, where R_M (~3396 km) is the radius of Mars. We set an energy threshold of $0.1E_{escp}$ for the definition of energetic particles, where E_{escp} is the escape energy of the neutrals (~2 eV for O at Martian surface). If an energetic particle losses its energy to less than $0.1E_{escp}$ after a collision, it is suppressed as a thermal one and ceased to trace the trajectory. This energy threshold is chosen for a balance between the calculation speeds and the density accuracy above ~700 km, since the O density is largely dominated by the thermal components below this altitude [*Chaufray et al.*, 2007]. Because only the collisions between energetic and thermal particles are considered, the heating of the upper atmosphere and the long range collisions are ignored in the sputtering model. Yet, the populations of the collided energetic particles ($> 0.1E_{escp}$) and their transportations can be determined. In addition to the escape rates, the sputtered hot corona above 700 km can therefore be deduced and compared with the UV emission measurements if detectable.

3. Case Comparisons on Precipitation and Sputtering Results

To provide an idea of the range of sputtering effects, we analyze six cases of different simulation results and compare them. These cases are chosen that the MHD or including the pickup ion tracing results are already published, and their simulation techniques as well as the model settings are consistent [*Ma et al.*, 2004; *Ma and Nagy*, 2007; *Fang et al.*, 2013]. The input solar wind parameters, solar cycle EUV level, and the crustal field assumptions are summarized in Table 1, with each case named by their special characteristics for comparisons. The quiet, active, and extreme cases are simulated with the strongest crustal field at noon under EUV intensity at solar maximum. Different solar wind parameters are utilized to see the effects from the interplanetary plasma. On the other hand, under solar minimum conditions the noonC, dawnC, and noC cases are subject to the same solar wind condition, but the strongest crustal field is set from the noon to the dawn side and switched off for the last one. Note that in all cases, the cross-flow (B_y) IMF orientations are pointing from dawn to dusk and the solar wind convection electric fields are directed toward north. In addition, no tilting of the Mars' spin axis is applied and the simulation results represent those at equinox. However, these examples give a general idea of both electric field hemispheric asymmetries and crustal field effects. Further case studies with different orientations of the IMF and seasonal variations will be needed in the future.

Table 2 summarizes the global average precipitation fluxes and energies for different cases. From a global point of view, both the enhancement of the solar wind and the EUV intensities can increase the pickup ion precipitation fluxes and average incident energies. Especially for the extreme case, the increase of the solar wind pressure and the IMF intensity not only produce more precipitating ions but also accelerate them to reimpact the upper atmosphere with significantly larger energies. Table 3 shows the sputtering escape

Table 2. The Resultant Pickup O^+ Precipitation Flux and Energies for Six Studied Cases

Cases	Average Precipitation Flux (cm^{-2} s^{-1}) Reimpact Rate/Ion Production Rate	Average Energy Flux (keV cm^{-2} s^{-1})	Global Average Incident Energy Day/Night
Quiet	6.4×10^6	3.9×10^5	60 eV
	65%		42/160 eV
Active	1.5×10^7	1.3×10^6	83 eV
	51%		81/88 eV
Extreme	5.0×10^7	2.5×10^7	486 eV
	62%		493/467 eV
NoonC	4.2×10^6	1.1×10^5	25 eV
	80%		17/72 eV
DawnC	3.4×10^6	7.0×10^4	20 eV
	75%		15/69 eV
NoC	2.7×10^6	9.3×10^4	35 eV
	67%		34/48 eV

rates for each species for different cases. Since the sputtering efficiency of producing the escape of neutrals increases with the incident pickup O^+ energies and reaches its maximum in the keV range [*Johnson et al.*, 2000] (see also Appendix A), the atmosphere loss rate as for the extreme case can reach about 50 times that of the nominal quiet case. More detailed comparisons between the quiet, active, and extreme cases can be found in *Wang et al.* [2014]. In short, for the active case, although larger solar wind speed can accelerate the pickup ions mainly in the upstream region, the divergence of the solar wind around Mars in the plasma sheath will dilute the precipitation fluxes on the hemisphere with outward pointing convection electric fields. However, the enhancement of the IMF can intensify both the ion reimpact rates and energies on the hemisphere with inward pointing electric field by reducing the picked up O^+ gyroradii. Therefore, the IMF strength is a more effective parameter for increasing sputtering efficiencies than the speed of the solar wind.

It is interesting to note that the recycling rates, i.e., the pickup ion reimpact rates divided by their total production rates near Mars, are similar for all three solar maximum cases, regardless of the variation of the solar wind conditions. However, they are significantly different from the recycling rate of the noonC case, which possesses the same crustal field orientation but is illuminated by EUV intensity at solar minimum. Although severe solar wind conditions can produce more pickup ions through electron impact and charge exchange, and enhance the precipitation flux simultaneously, the major ion production mechanism is still photoionization. Therefore, the mass loading to the solar wind is similar for the same EUV intensity. This will cause approximately equivalent pickup ion recycling rates. However, as the scale height of the neutral atmosphere and the number density in the hot corona increases with the solar EUV intensity due to greater heating and more photochemical reactions, the ionosphere can stand off the solar wind and the magnetic pileup boundary (MPB) further above the surface [*Ma et al.*, 2004]. Thus, it becomes more difficult for the pickup ions to reach the exobase region, resulting in less recycling rates for the solar maximum cases [*Chaufray et al.*, 2007]. Although the pickup ion recycling rate can increase with the decrease of the solar EUV intensity, the total ion production rate decreases leading to less pickup ion precipitation rates. With a more tenuous hot corona (see Figure 1) and smaller photoionization rates, the pickup O^+ production rates for the noonC case decreases to 50% of that of the quiet case, and the ion precipitation rate also reduces to about 66% for the solar minimum one. In addition, with less ions produced at higher altitudes, the average incident ion energy

Table 3. The Global Escape Rates and Yields for Six Simulated Cases

Escape (s^{-1})	O	CO_2	CO	C
Quiet	2×10^{24} (16%)	9×10^{21} (0.08%)	4×10^{20} (0.003%)	2×10^{23} (2%)
Active	4×10^{24} (14%)	2×10^{22} (0.07%)	1×10^{20} (0.0005%)	2×10^{23} (0.6%)
Extreme	1×10^{26} (113%)	4×10^{23} (0.6%)	2×10^{23} (0.02%)	8×10^{24} (10%)
NoonC	5×10^{23} (8%)	4×10^{21} (0.06%)	1×10^{20} (0.002%)	6×10^{22} (0.8%)
DawnC	3×10^{23} (6%)	2×10^{21} (0.04%)	9×10^{19} (0.002%)	4×10^{22} (0.7%)
NoC	5×10^{23} (11%)	4×10^{21} (0.08%)	9×10^{19} (0.002%)	6×10^{22} (1%)

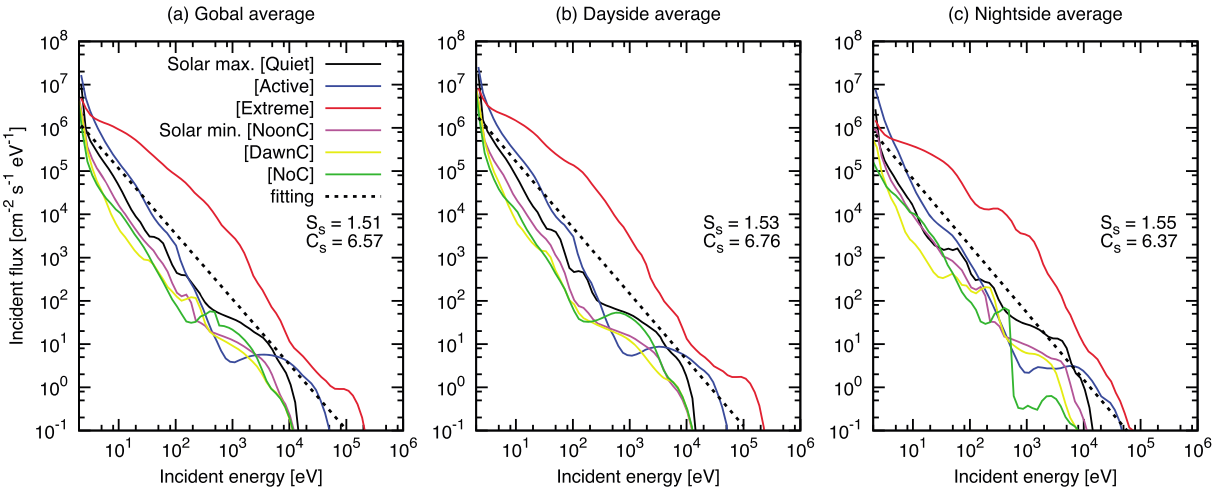

Figure 2. The (a) global, (b) dayside, and (c) nightside averages of the pickup O^+ incident energy spectra for the simulated cases. The fittings representing all six cases in one slope are also shown for different average values in each panel. The fitting parameters C_s and S_s are the fitted flux at $E = 1$ eV and the fitted slope, respectively.

also decreases. As a result, the sputtering escape rate of O decreases to only about 25% of the nominal solar maximum value as shown in Table 3.

The escape yields, which are the escape rates divided by the total pickup O^+ precipitation rates, are also included in the brackets in Table 3. The escape yields can be related directly to the incident ion energies and angles. Although the incident angle with respect to the surface normal axis can also influence the sputtering efficiencies [*Johnson et al.*, 2000], the precipitation energy plays the key role on the sputtering yields and can significantly vary with different solar wind conditions and EUV intensities. In addition to the average incident energies shown in Table 2, we also analyze the energy spectra of the incident pickup O^+ in more detail. Figure 2 shows the global, dayside, and nightside average energy spectra for the six cases. The black dashed lines represent the fitted slopes for all results. The weightings of the fitting are 0.25 for each of the four cases under nominal solar wind conditions and 1 for the active and extreme ones. In this way, the fitted slope takes into account the variation of the interplanetary plasma since we only have two cases simulating the changeable solar wind interactions. We fit the spectra with the formula

$$f(E) = C_s E^{-S_s} \tag{2}$$

where E is the ion energy, $f(E)$ is the differential flux, and C_s and S_s are the fitted flux at $E = 1$ eV and the fitted slope, respectively. With the fitted slope, we can have a basic idea about the energy distribution of the reimpact pickup O^+. Except for the extreme case, other case results show certain depletions in the medium energy range for the average spectra. As indicated in the dayside average spectra, the depletion occurs primarily on the hemisphere of the upstream side of the solar wind. This is because the upward pointing electric fields and the surface crustal fields can shield the ions with medium energies from reimpact more easily [*Wang et al.*, 2014]. On the other hand, about or less than one quarter of the reimpacting ions precipitate on the nightside. The energy spectra on the nightside show different patterns than those at dayside. They are more similar to a fitted slope with less depletion at medium energy range than in the dayside spectra. When the crustal field lines are draped to the nightside to contribute to the magnetic tail, the magnetic fields can capture the pickup ions and drive them to move upstream toward Mars [*Li et al.*, 2011; *Wang et al.*, 2014]. Therefore, the role of crustal fields become an assist for the re-impact of the pickup ions rather than reflecting and shielding of the medium energy ions as on the dayside. However, the ions produced at higher altitudes may have difficulty reimpacting the atmosphere downstream, leading to fewer higher energy ions precipitating on the nightside. Combining the depletion of medium energies on the dayside and fewer high energy ions on the nightside, the fitted slope in the global averages have smaller S_s (Figure 2a) than the two hemispheric average ones (Figures 2b and 2c). Nevertheless, for the extreme case with much stronger IMF strength, the ions at lower altitudes can be accelerated toward medium energies when they reimpact to the atmosphere. An obvious hump in the medium energy range appears in the spectra and the average incident energy increases to about 500 eV as shown in Table 2.

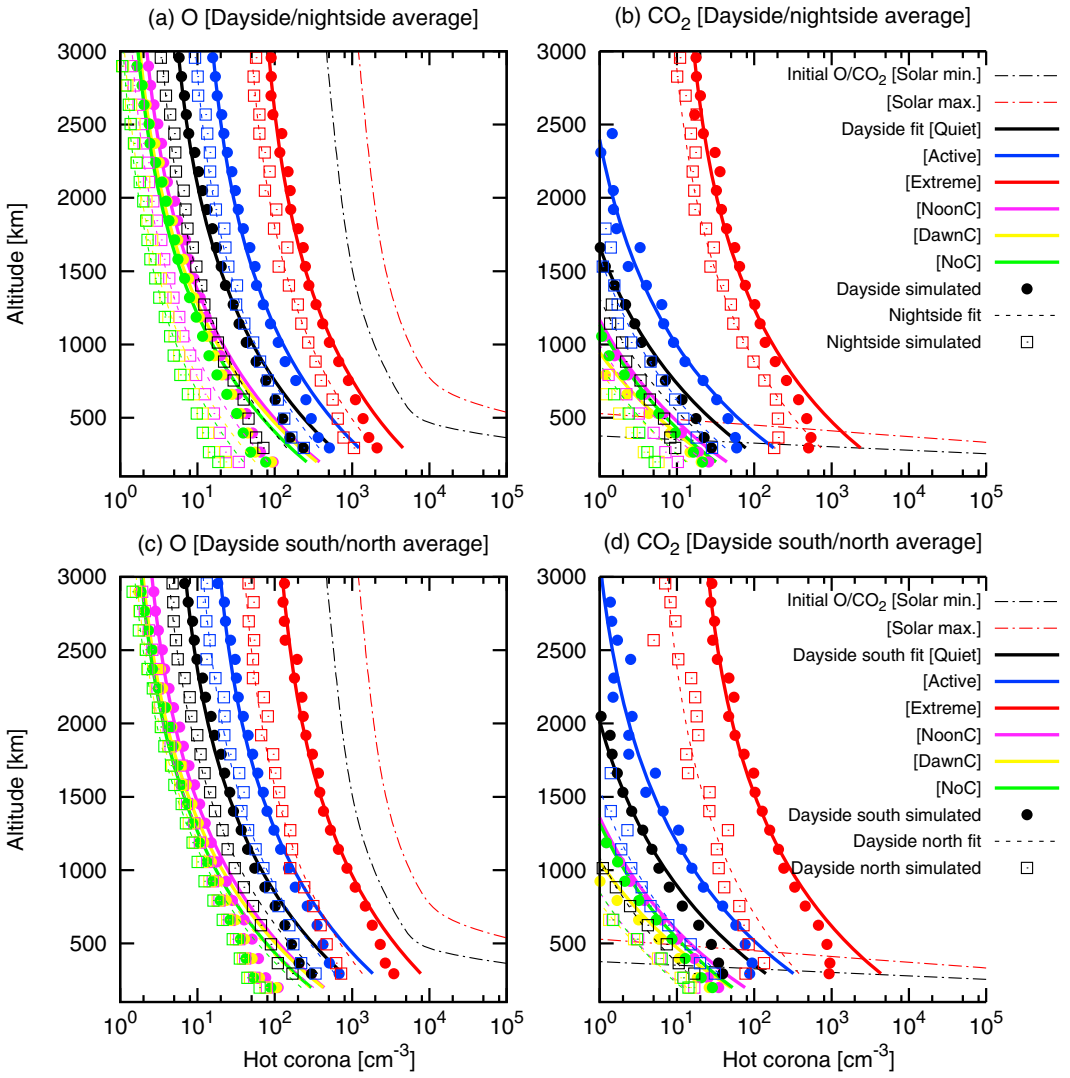

Figure 3. The regional averages of the sputtered hot corona distributions of O and CO_2 for different cases. The average values of the dayside, nightside, dayside southern hemisphere, and dayside northern hemisphere are shown for comparisons. The fitting slopes are also shown with the simulated data. The initial background O and CO_2 profiles as plotted in Figure 1a are displayed with dash-dotted lines as references.

In addition to the sputtering effects causing escape, the incident energetic ions can also produce gravitationally bound neutrals with higher energies than thermal. Figure 3 shows the hemispheric average sputtered hot O and CO_2 corona distributions for the six cases. Again, fitted profiles are also shown with different colored solid and dashed lines. The altitude distribution of the density $n(r)$ are fitted with fixed temperature T as

$$n(r) = n_0 \exp[-(r - r_0)/H(r)] \tag{3}$$

$$H(r) = \frac{kT}{mg(r)} \tag{4}$$

where r is the distance from the center of Mars, n_0 is the reference density at reference distance r_0, $H(r)$ is the scale height at distance r, k is the Boltzmann constant, m is the mass of the fitted species, and $g(r)$ is the gravitational acceleration at r. Since we set an energy threshold of $0.1E_{escp}$ for the traced particles in the model, the densities at altitudes $<$ 700 km will be underestimated as described in section 2. As the densities at higher altitudes will take longer simulation times to reach a saturated state, we fit the density

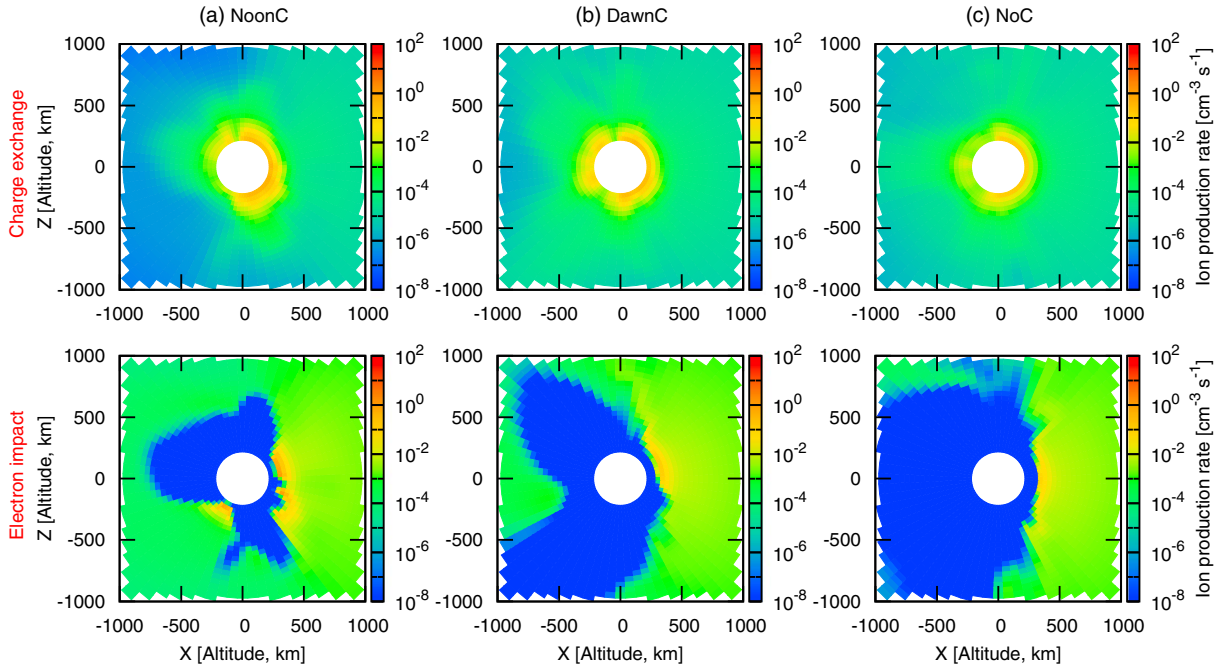

Figure 4. The pickup ion production rates from charge exchange and electron impacts in the noon-midnight cutplane for three solar minimum cases. The Sun is to the right of the figure. Note that Mars itself is represented as a point (not to scale) in the center of each panel in order to provide a better view of the distributions at lower altitudes. Note that the absence of the data below the lower boundary of the pickup ion model (200 km) forms a white disk in the center of each panel, which is not Mars itself.

distributions only between 1000 and 3000 km. In addition, the fitted profiles can provide better estimations of the densities at lower latitudes (< 700 km) than the simulation results. For the sputtered hot O corona, the density is normally smaller than the hot components from the dissociative recombination of O_2^+ (dash-dottted lines in Figure 3) under nominal solar wind conditions. Although as the EUV intensity increases, the sputtered hot neutral densities can also be enhanced, the photochemical reactions become more dominant simultaneously. As a result, it is still difficult to detect the sputtered O corona. On the other hand, as the solar wind becomes disturbed, the sputtered corona density can increase as well. For the extreme case, the sputtered corona density can reach about 10^3 cm^{-3} for both O and CO_2, which might be detectable by the instruments. In some specific regions of the inward pointing electric field hemisphere (south in the present case) on the dayside, the O density can even become comparable to that from the dissociative recombination of O_2^+ as indicated in *Wang et al.* [2014].

Aside from the external drivers including the solar wind and the EUV intensities, the effect of the surface crustal field is relatively minor in altering the sputtering effects when comparing the three solar minimum cases. This is contrary to what was suggested by *Li et al.* [2011], who proposed that the draped magnetic fields on the nightside can preserve more pickup ions to reimpact the upper atmosphere, and this consequence could induce more sputtering. In fact, the precipitating flux does increase when the strongest crustal fields face directly into the solar wind as shown in Table 2. However, the resultant sputtered escape rates and the hemispheric average hot corona densities do not change significantly.

Figure 4 shows the ion production rate distributions on the noon-midnight plane from charge exchange and electron impact for the three solar minimum cases. We can see that as the crustal fields can confine more ions and electrons at lower altitudes, the pickup O^+ production rates become more efficient near the surface. For the electron impacts, the pickup ion production rates reach a peak value as the electron temperature increases to above 10^6 K [*Cravens et al.*, 1987]. If there is no crustal field on Mars surface or the field is weak on the dayside, the solar wind electrons will be shielded above the MPB and produce pickup ions mainly in the plasma sheath. As the crustal field strength increases on the upstream side, the interaction with the IMF can allow the solar wind electrons to leak into the cusp regions (where open field lines allow their entry) toward the surface and produce more pickup ions at lower altitudes.

Table 4. The Ion Production and Precipitation Rate Comparisons for Three Solar Minimum Cases With Different Surface Crustal Field Distributions

	NoonC		DawnC		NoC
Precipitation rates	1.6	:	1.3	:	1
Day/night precipitation	84%/16%		90%/10%		91%/9%
Total production rates	1.3	:	1.1	:	1
Charge exchange (s^{-1})	2.5×10^{24} (29%)		2.3×10^{24} (31%)		1.5×10^{24} (23%)
Electron impact (s^{-1})	1.6×10^{24} (19%)		7.1×10^{23} (10%)		6.4×10^{23} (10%)
	Ion Production Rates		Below 500 km		
Charge exchange	1.6	:	1.5	:	1
Electron impact	12.4	:	2.0	:	1
Total	1.3	:	1.1	:	1
	Ion Production Rates		Above 500 km		
Charge exchange	1.0	:	1.3	:	1
Electron impact	0.8	:	1.0	:	1
Total	0.9	:	1.0	:	1

Table 4 shows the comparisons of the ion precipitation rates and production rates at different regions from charge exchange and electron impact for the three solar minimum cases. Under the influences from different crustal field distribution, the variation of the ion production rates occurs mostly at altitudes below 500 km. The values in the brackets in Table 4 show the percentage of each production rate compared to the total rates including photoionization. Although the production rate from electron impact can increase more than 1 order of magnitude at lower altitudes for the noonC case, their contribution to the total rate is still relatively small. When the ion production rate for the case with the strongest fields facing the Sun increases by 1.3 times of that of the noC case, the precipitation rate can increase by 1.6 times comparing to the case without crustal fields. Thus, when the crustal field located on the dayside, pickup O^+ precipitation rate can be enhanced in addition to the increasing production rate. This is because the closed crustal field lines can not only confine more ions produced at lower altitudes but also the trapped pickup ions more easily reimpact the upper atmosphere. The dayside and nightside precipitation portions are also presented in Table 4 for different cases. As indicated in *Li et al.* [2011], there are more pickup ions precipitating on the nightside as well as dayside for cases with crustal fields than without them.

Although the global pickup ion precipitation rates and average incident energy on the nightside do increase when the strongest crustal fields face directly into the solar wind as summarized in Table 2, the average reimpacting energy on the dayside actually decreases. Figures 5a and 5b (top) show the spectra of the cases with crustal fields divided by that without crustal fields, and Figures 5a and 5b (bottom) show the inverse values with inverse *y* axis for the ratios. We can see clearly that on the dayside hemisphere, more reimpacting ions precipitate with lower energies from lower altitudes for the case with stronger crustal fields in the dayside. Moreover, the crustal field can prevent reimpact from ions produced at higher altitudes, leading to large depletion of the keV range of precipitating ions. Although the situation is opposite on the nightside within the draped magnetic fields downstream, those contributions to the total precipitation rates are only about 16% or less (see Table 4). Overall, under the influence of the crustal fields the shortage of the keV range ions decreases the sputtered escape rates and the formation of the hot corona from the larger precipitation fluxes. When the strongest crustal fields are located on the dawnside, the sputtered escape rate becomes even smaller than that without the crustal fields. With the reduction of the precipitation from the higher-energy particles, the existence of the crustal fields actually diminishes the sputtering escape efficiencies.

4. Sputtering Response Relations

In spite of the fact that the precipitation flux and the energy and angle distributions of the pickup ions can vary at different locations and be altered with the solar wind, the EUV intensity and the Mars environments, we can still develop a statistical approach to sputtering effects that can be used as related measurements become available. If we integrate the collisional frequency as calculated in equation (1) along the trajectories of the incident particles with the mean free path ($l = 1/(n_{th}\sigma_T)$), the energetic particles produced by the

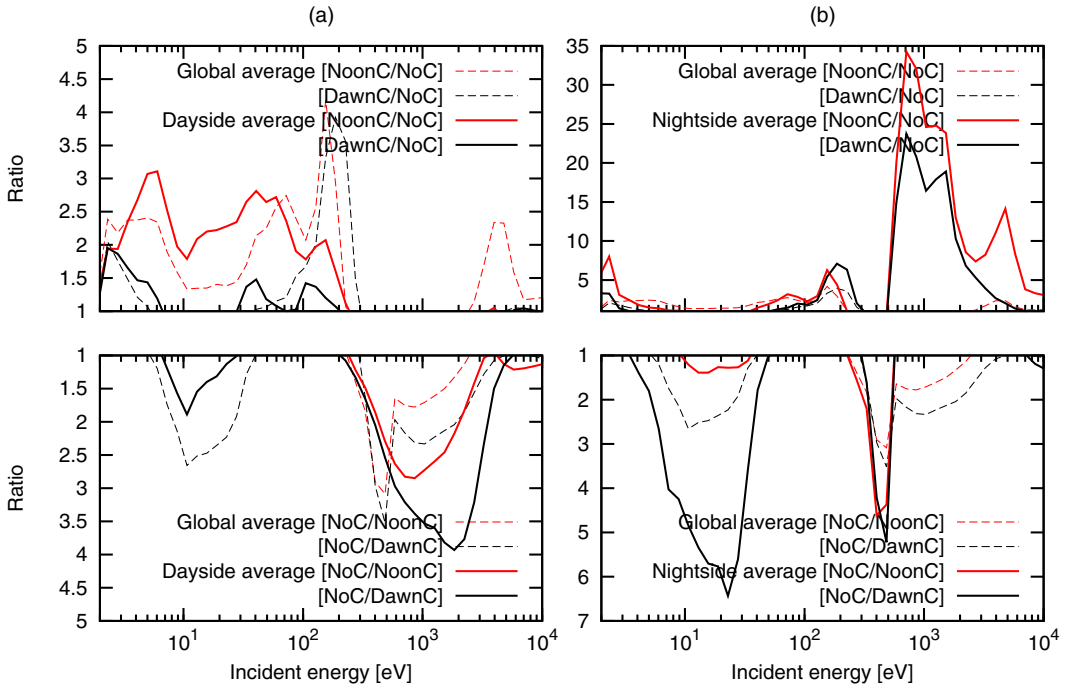

Figure 5. The (a) dayside and (b) nightside average incident energy spectra comparisons of the pickup O^+ for three solar minimum cases. The global average ones are also shown in dashed lines in both figures. They are derived from those shown in Figure 2 for the solar minimum cases. The top shows the values when the two cases with crustal fields divided by the one without surface remnants. The bottom shows the inverse values (NoC case divided by the other cases with crustal fields) with inverse *y* axis. Since the ranges of the *y* axes in Figures 5a and 5b are different, the global average values can be treated as a reference for comparisons between dayside and nightside ones.

incident ions in the integrated column can be derived as

$$F_{cl} = \frac{1}{2} n_i \bar{V}_i \tag{5}$$

where n_i and $\bar{V}_i$ are the number density and average velocity of the incident ions. Note that the background isotropic thermal velocity $\bar{V}_{th}$ becomes zero on averaging. As a result, the integrated collisional frequencies will not be influenced by the structure of the atmosphere, such as the scale height of the density and the temperature. However, the relative collisional rates for each species will be different according to its mixing ratio near the exobase region and the relative cross section. Here we introduce a factor A' including the effects of the cascade collisions, ratios to the upward flux, species mixing ratios, and their relative cross sections. Then the upward flux of species *s* induced by the sputtering of the incident ions can be calculated as

$$f_{s\uparrow} = \frac{1}{2} A'_s n_i \bar{V}_i \tag{6}$$

As we assume that the downward flux is equal to the upward flux in the calculated cell, the average number density of the incident ions can be derived with their incident flux *f* and the average upward velocity $\bar{V}_{i\uparrow}$ as

$$\bar{n}_i = f/\bar{V}_{i\uparrow} = A_{s0} f/\bar{V}_{s\uparrow} \tag{7}$$

Through the cascade collisions and the energy exchange to the neutrals, the velocity of the incident ions can be transferred into that of the recoiled neutrals with an proportional factor A_0. Therefore, the sputtered upward flux of each species can be related to the flux *f* and the average energy $\bar{e}$ ($= \frac{1}{2} m_i \bar{V}_i^2$) of the incident ions as

$$f_{s\uparrow} = \frac{1}{2} A_s \sqrt{\bar{e} f^2} / \sqrt{\frac{1}{2} m_i \bar{V}_{s\uparrow}^2} \tag{8}$$

where $A_s = A'_s A_{s0}$ and m_i is the mass of the incident ion. In this way, we can estimate the sputtered hot corona number density n_0, column density N_c and the escape flux F_{escp} as

$$n_0 = f_{s\uparrow}/\bar{V}_{s\uparrow} = \frac{1}{2}A_s\sqrt{\bar{e}f^2}/\left(\sqrt{\frac{1}{2}m_i\bar{V}_{s\uparrow}^2}\right) \tag{9}$$

$$N_c = n_0 H = n_0\left(\frac{1}{2}\bar{V}_{s\uparrow}^2/g\right) = \frac{1}{4}A_s\sqrt{\bar{e}f^2}/\left(\sqrt{\frac{1}{2}m_i g}\right) \tag{10}$$

$$F_{escp} = B_s f_{s\uparrow} \tag{11}$$

Again, we introduce a proportional factor B for the escape ratios to the total upward flux for each species s.

As discussed above, we found that the sputtered hot corona density and the escape flux are proportional to the incident flux and the velocity. We plot the resultant sputtered components at different locations versus the square root of the incident number flux multiplied by the incident energy flux ($\sqrt{f \times f_e}$) for each case with smaller colored symbols in Figure 6. When the incident flux f can be calculated from the integration of the incident energy spectrum $f(E)$ as

$$f = \int f(E)\mathrm{d}E \tag{12}$$

the energy flux f_e is calculated as

$$f_e = \int Ef(E)\mathrm{d}E \tag{13}$$

We can see that the plotted symbols indeed follow certain relations in log scale but much scatter exists for several reasons. One reason for the scatter is from the represented average incident energy $\bar{e}$ included in the energy flux f_e. As discussed in section 3, different energies of incident ions will lead to different efficiency for their sputtering. This cannot be precisely represented with an average value. Although the average energy spectra shown in Figure 2 are more or less continuous, the incident energy distributions at different locations can have gaps in various energy ranges [*Wang et al.*, 2014]. Therefore, spectra with very different kinds of distributions may lead to the same represented average energy $\bar{e}$. Also, the differences in the incident angles can play a role. Since the orientation of the collisional process can lead to different scattering angles with respect to the surface normal axis, the upward flux will be modified by different precipitation angles of the ions. As for the hot corona distribution, the transport of the neutrals will smooth out the density distributions between nearby locations, leading to the departure of the connections with the incident ion flux and energies at the specific precipitation site. Moreover, the limitation of the simulated test particles in the model will induce statistical fluctuations in the results, especially for the dissociated CO and C. Therefore, we average out the values into eight sections globally for each case in order to derive better relations as shown with larger black symbols in Figure 6. In this way, the results derived from the average incident energies and angular distributions become smoother and more similar to each other. The represented average energy $\bar{e}$ then more closely represents a continuous spectrum. At the same time, the effects from the transport of the particles and the fluctuations due to the limitation of numbers of simulated particles can be minimized.

We fit a "sputtering response relation" between the incident pickup ions and the sputtered hot components with an equation

$$\log F_v = S\left(\log\sqrt{f \times f_e}\right) - C \tag{14}$$

where F_v is the fitted sputtering value including the corona density (n_0 and N_c) and the escape flux (F_{escp}), S and C are the fitted slope and the fitted lower cutoff value. As indicated in section 3, we also use different weightings for different cases for the sputtering response relation fittings in order to include the effects of the solar wind variations. The fitted results are plotted with black solid lines in Figure 6. The standard deviations $\bar{\varepsilon}$ are also shown with dashed lines, which are calculated from the values shown by the colored

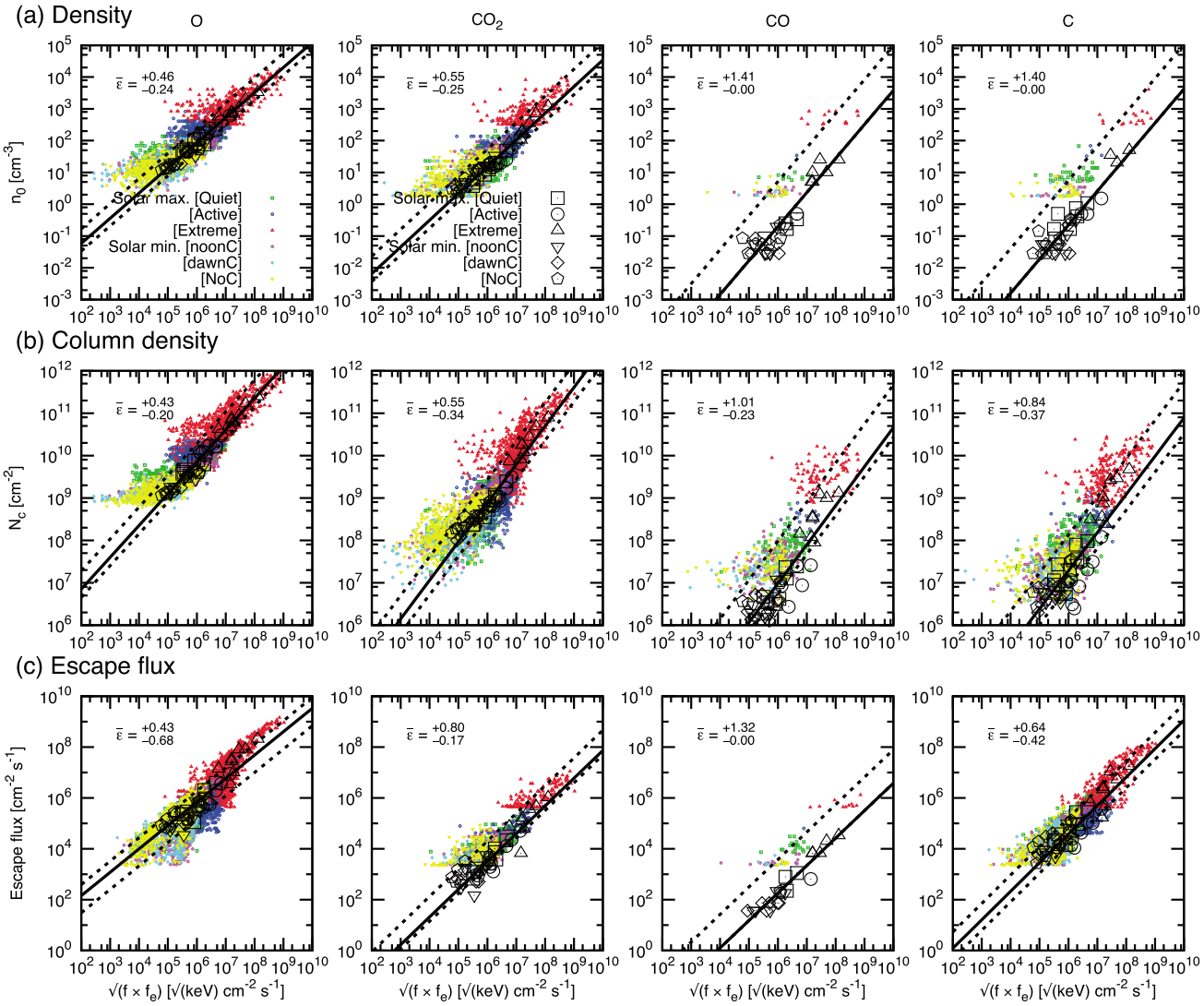

Figure 6. The sputtering response relations for sputtered O, CO_2, CO, and C with incident pickup O^+. The *x* axis is the square root of the incident pickup O^+ fluxes multiply with their energy fluxes, and the *y* axes show (a) the sputtered hot corona number densities at 200–300 km, (b) column densities above 200–300 km, and (c) escape fluxes, respectively. The smaller colored symbols are the simulated data at different latitudes and longitudes, and the larger black symbols are the average values in eight portions globally. The fitting slopes of the sputtering response relations are also shown with thick black lines with standard deviation ($\bar{\varepsilon}$) in dashed lines in each panel. Note that the standard deviation values are calculated in logarithm.

symbols without averaging. It is interesting to note that for the extreme case, some of the sputtering responses show deviations from the fitted relations toward the positive standard deviations, such as for the escape flux of O. This is because the energy spectra for the extreme case exhibits humps in the medium energy range (see Figure 2), which leads to a larger contribution at higher energies of the incident ions compared to the other cases and causes the deviations in the fitted relations.

As discussed in section 2, the sputtered corona density is underestimated below 700 km from our simulations. The fitted sputtering response relations of the simulated corona reference density at the upper boundary of the collisional domain and the integrated column density above it introduce certain errors due to the setting of our model. Therefore, we fit the corona density profiles for the eight averaged sections similar to those shown in Figure 3 and fix the reference altitude at 1000 km. The integrated column density is also replaced by the fitted reference number density multiplied by the scale height at 1000 km. The sputtering response relations for the fitted corona are shown by red symbols with the fitted relations shown as red lines in Figure 7. Because the fitted reference densities are from higher altitudes than the upper boundary of the collisional domain in the model, they are smaller than the simulated results

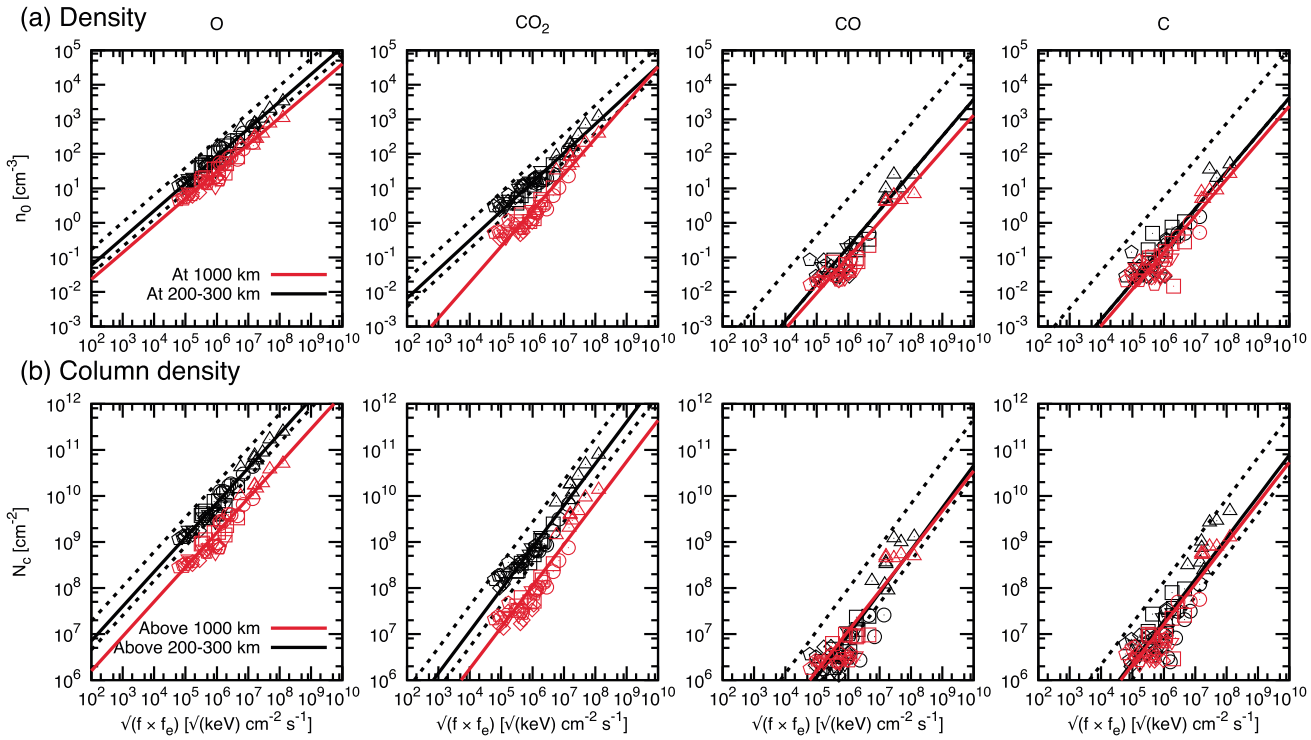

Figure 7. The sputtering response relations for the sputtered hot corona distributions. The black-colored symbols and fitting lines show the original simulated data as in Figure 6, and the red ones are from the fitted corona values with reference altitude at 1000 km. Some examples of the fitting corona are shown in Figure 3.

at ~200–300 km. Since the scale height will increase with the altitude due to smaller gravitational acceleration further away from Mars' surface, the integrated column densities up to the upper boundary of the collisionless domain (3 R_M from the center in our model) are also larger than the integration with a fixed scale height fitted at 1000 km. The slope of the sputtering response relation of the reference number density of CO_2 becomes steeper for the fitted values since the scale height of the hot corona is smaller for smaller incident flux and energy due to its larger mass.

Table 5 summarizes the fitted slopes S and the fitted lower cutoff values C of the sputtering response relations for the fitted corona density n_0 and n_0H at 1000 km and the escape flux F_{escp} for each species. Note that the fitted values are in cgs units, but the energy is in keV. With these sputtering response relations, we can provide quick estimations of the sputtering effects from the incident energy spectrum of the pickup O^+ from measurements or other simulation results. As equating the fitted relations (equation (14)) to the derived equations (9)–(11), we can also calculate the average proportional factors A, $\bar{V}_\uparrow$, and B for different incident ion fluxes and energies. We should be careful that the derived equations (9)–(11) are based on the assumption of a collective average behavior of the sputtering process and do not take into account the nonisotropic sputtered fluxes and the nonlinear effects of the recoils. However, we can still learn some general concepts hidden behind the fitted "sputtering response relations" from these average proportional factors in a gross point of view.

Table 5. The Fitting Parameters of the Sputtering Response Relations for Each Species

Fit Values	Parameters	O	CO_2	CO	C
n_0	S_1	0.78	1.04	1.03	1.06
	C_1	3.19	5.88	7.18	7.22
n_0H	S_2	0.75	0.90	0.87	0.88
	C_2	−4.70	−2.64	−1.84	−1.93
F_{escp}	S_3	0.92	1.09	1.08	1.12
	C_3	−0.32	3.04	4.22	2.15

The sputtering efficiency A for producing the upward flux can be directly calculated from the column density relations (n_0H). With known parameter A, the average upward velocity $\bar{V}_\uparrow$ and escape ratio B can be subsequently determined. Table 6 shows the resultant

Table 6. Derived Sputtering Parameters Form the Sputtering Response Relations

	O			CO_2		
$\sqrt{\bar{e}f^2}$ ($\sqrt{\text{keV}}$ cm^{-2} s^{-1})	10^3	10^5	10^7	10^3	10^5	10^7
A above 1000 km	1.15	0.36	0.11	0.03	0.02	0.01
$\bar{V}_\uparrow$ (km/s) at 1000 km	2.12	1.98	1.85	2.98	2.16	1.56
B	1.24%	2.47%	4.93%	0.03%	0.07%	0.19%

proportional factors for O and CO_2 from the fitting relations in Table 5. As the fitted slopes S_2 for the column density n_0H are smaller than 1, the sputtering efficiency of producing the upward flux A decreases with incident ion flux and energy. When $\sqrt{\bar{e}f^2}$ is equal $10^3\sqrt{\text{keV}}$ cm^{-2} s^{-1}, A is larger than 1 for O. This means that the cascade collisions produce more ejected O. However, as $\sqrt{\bar{e}f^2}$ increases, the cascade collisions may produce more neutrals directed downward toward the surface and the efficiencies for ejecting energetic neutrals to higher altitudes decrease. This is because when the energy of an incident ion is larger, the ion can penetrate deeper into the atmosphere and the recoiled particles will be produced at lower altitudes. As the thermalization through collisions with the background atmosphere is more efficient at lower altitudes, the related sputtered upward flux is reduced for the incident ions with larger energies. This process is also reflected by the derived average upward velocity $\bar{V}_\uparrow$, which decreases as well with increasing $\sqrt{\bar{e}f^2}$. As we compare the values with those of CO_2, the upward flux efficiency A is much smaller than that for O due to its larger mass, but the average upward velocity is comparable with a value of $\sim$ 2 km/s.

The ultimate goal is to know how the incident pickup O^+ affects the loss of the atmosphere. As indicated in *Johnson and Luhmann* [1998], an ion incident on the upper atmosphere can produce recoil particles with a spectrum having an energy tail decay as E^{-2}. Only at the higher-energy ends are the recoil particles energetic enough to escape. Collectively, less than 5% of the O upward flux produced by sputtering can escape and no more than 0.2% for CO_2. If we integrate the fitted global average energy spectrum for the six cases (see Figure 2 with a slope of 1.51) with equation (2) from a lower cutoff energy 0.1 eV to infinity, the flux with energies larger than 2 eV is about 22%. This means that most of the incident O^+ energies are deposited in the upper atmosphere or the ejected corona, while less than 5% of the sputtered upward O are able to escape. These numbers do not include consideration of any feedback effects, however, as newly created coronal O from the sputtering can be ionized and further added to the precipitating O^+ flux.

5. Discussions

With the fitted parameters of the sputtering response relations shown in Table 5, we can easily estimate the sputtered hot components (n_0 and n_0H at 1000 km, and F_{escp}) with equation (14) after calculating the incident pickup O^+ number flux and energy flux from the measured or simulated energy spectrum with equations (12) and (13). The sputtered neutral number density distribution between 1000 and 3000 km can be estimated from the derived reference density n_0 and scale height H at $r_0 = R_M + 1000$ km with equations (3) and (4). As discussed in section 4, the fitted relations are better correlated for an averaged continuous energy spectrum. Therefore, we suggest using the relations for the average spectrum measured from a single spacecraft pass, statistical measurements, or for hemispheric averages from simulations. With gaps or discontinuous smoothed out in the assumed incident energy spectrum, the derived hot corona and escape flux from the fitted sputtering response relations can be used to get better estimations of the average values for the chosen region. For example, the fitted slope S_s (see equation (2)) of the total 48 average spectra from our simulations (eight sections for each case) ranges from 1.29 to 1.90. One can also fit their average spectra to determine if it is appropriate to use the present derived fitted relations from our six case studies. In this way, the uncertainties derived from using the average incident pickup O^+ flux and energy with the sputtering response relations can be minimized.

The SupraThermal and Thermal Ion Composition (STATIC) instrument onboard MAVEN is able to measure O^+ pickup ion spectra near Mars. Before we use those data to calculate the detailed sputtering effects with an atmospheric sputtering model, we can quickly estimate their average or the overall efficiencies statistically through the sputtering response relations. The coronal sans from the Imaging Ultraviolet Spectrometer (IUVS) can determine the hot oxygen density and distributions below about 3000 km altitude. However, the measured exospheric densities include the contributions from various sources, such as dissociative recombination of O_2^+, etc. As the sputtered component from the pickup O^+ can be evaluated

Table 7. The Interpolated Ancient Sputtering Atomic Escape Rates for O, CO_2, CO, and C From the Sputtering Response Relations and the Comparisons With Previous Studies

Epochs	1 EUV (Present)	3 EUV (2.5 Gyr Ago)	6 EUV (Very Early Epoch)
Increment of $\sqrt{\bar{e}f^2}$[a]	1	252 × 1 EUV	4200 × 1 EUV
Nominal solar minimum	6×10^{23} s^{-1}	1×10^{26} s^{-1}	1×10^{27} s^{-1}
	|	|	|
Extreme solar maximum	3×10^{25} s^{-1}	6×10^{27} s^{-1}	9×10^{28} s^{-1}
Luhmann et al. [1992]	1×10^{24} s^{-1}	4×10^{26} s^{-1}	4×10^{27} s^{-1}
Leblanc and Johnson [2001]	7×10^{23} s^{-1}	1×10^{26} s^{-1}	-
Leblanc and Johnson [2002]	6×10^{23} s^{-1}	2×10^{26} s^{-1}	2×10^{27} s^{-1}
Chaufray et al. [2007]	$2–7 \times 10^{23}$ s^{-1}	-	-

[a]From *Johnson and Luhmann* [1998] and *Leblanc and Johnson* [2002].

from the STATIC measurements and the sputtering response relations, comparisons with other hot sources and the correlations with the detected profiles from IUVS can provide us further information about the chemical and physical processes in Martian upper atmosphere.

From the fitting relations, we can also interpolate the sputtering related atmospheric loss rates to ancient Mars which requires a wider range of solar wind parameters, solar EUV intensities, and Mars diurnal and seasonal variations. For example, Table 7 shows the estimated increment of $\sqrt{\bar{e}f^2}$ from *Johnson and Luhmann* [1998] and *Leblanc and Johnson* [2002], and the interpolations of the atomic escape rates of all O- and CO_2-related components from the present six simulation results to ancient epochs. The calculated results from previous studies are also shown for comparisons. We can see that they are in good agreements within an order of magnitude under nominal solar minimum conditions. In addition, we can extend our results to various levels of solar activities and different Mars environments with the relations. Since the primitive Sun is supposed to have been more active than present, the impact of the related dynamic processes on sputtering effects is important to understand.

Yet we have to remember that this kind of interpolation is based on the assumption that the global average incident pickup O^+ energy spectrum can be approximately fitted with a slope (equation (2), also Figure 2). If the incident pickup ion energies are described by very different spectra, the simplified interpolation will break down with larger deviation from the present relations. Also, different mixing ratios of neutral species near the exobase region can introduce uncertainties due to different sputtering cascade collisional processes. In our six simulations, the O/CO_2 mixing ratios near the exobase are 0.1 and 0.3 for solar minimum and solar maximum atmospheres, respectively. In fact, since O is lighter than CO_2 and should have larger escape rates, the O/CO_2 mixing ratio would increase toward earlier epochs. *Zhang et al.* [1993] and *Johnson and Luhmann* [1998] suggested that at 3 EUV epoch (~ 2.5 Gyr ago), the O/CO_2 mixing ratio can increase to more than 0.4 and even reach 4 at 6 EUV epoch (very early epoch). However, we can still overcome these uncertainties after adding more simulation results into the fittings of the sputtering response relations in the future.

It is interesting to note that the sputtering escape rates derived by *Chaufray et al.* [2007] showed the lowest value between all the results listed in Table 7. Since they used a more realistic 3-D hot O exosphere, the global pickup O^+ production rates become smaller than those derived from uniformly distributed 1-D profiles. While *Chaufray et al.* [2007] did not include the surface crustal fields in their hybrid model, their low solar activity case is more similar to our NoC case. After comparing those two cases, we can see that from our NoC case the total O^+ production rate, the pickup ion precipitation rate, and the sputtering atomic escape rate are about 3.7, 2.7, and 3.5 times larger than those of their low solar activity case, respectively. In addition to the differences between their hybrid model and our MHD and pickup ion tracing models, they used a pure O atmosphere instead of a CO_2 dominant one in their atmospheric sputtering model. This means that every one CO_2 molecular is replaced by three O in the upper atmosphere in their initial settings. Nevertheless, the major influence on the global sputtering escape rates comes from the initial exospheric O densities, since all the O and O^+ related rates decrease simultaneously with the implementation of the 3-D exosphere when comparing our the results with those of *Chaufray et al.* [2007]. Therefore, we may overestimate the global rates by a factor of 2–4 when using a simplified spherically symmetric exosphere.

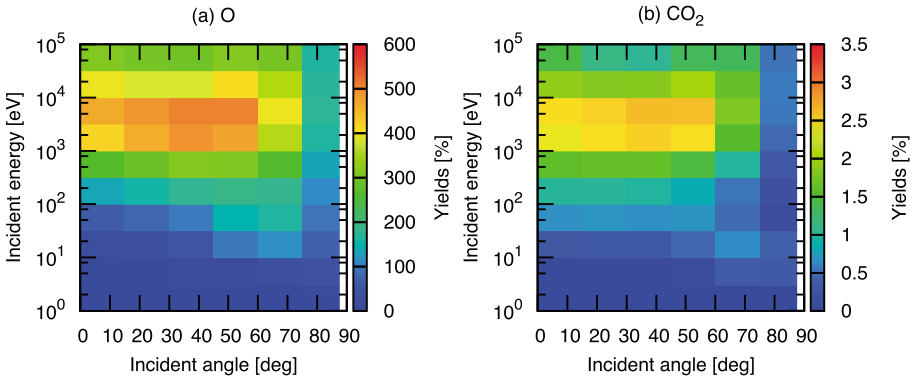

Figure A1. The sputtering escape yields with an incident O^+ for different fixed incident energies and angles for O and CO_2.

Thus far, we have learned from our six case comparisons that changes in the external solar wind and IMF can significantly change the pickup O^+ precipitation flux and energy as well as the sputtering efficiencies. The solar EUV intensity can also have influences but the dominant nonthermal source of dissociative recombination of O_2^+ can obscure the importance of the sputtering effects for the creation of hot O. On the other hand, the surface crustal field orientation has relatively small influences compared to the external drivers on a global scale. Additional simulation studies with different seasons and different IMF directions will be needed to learn more about their effects on the sputtering efficiencies. In addition, more realistic 3-D atmospheres should be implemented to study their solar wind mass loading effects, the influences on the pickup ion precipitation rates, and the resultant sputtering efficiencies. With the help of the measurements from the upcoming MAVEN mission, we will better constrain our simulation results as well as the derived sputtering response relations. Modeling the process in the present Mars environments can help us interpolate the sputtering effects to early epochs and lead to better understanding of its role in Mars atmospheric evolution.

Appendix A: Sputtering Tables

In addition to the "sputtering response relations," we also provide an alternative method to estimate the sputtered escape rates and the hot corona distributions. We use the atmospheric sputtering model for incident O^+ with fixed energy and angle (with respect to the normal axis of the surface) to build up 13 (energies) × 7 (angles) sputtering tables for the solar maximum atmospheres. The results are organized to represent the escape rates and the hot corona density produced by one incident O^+. Figure A1 shows the sputtered escape yield tables for O and CO_2. We can see that for lower incident energies, the escape yield is larger with larger incident angle. This means that the glancing ions can kick out more neutrals in the upper atmosphere toward higher altitudes where they can escape [*Johnson et al.*, 2000; *Leblanc and Johnson*, 2001]. However, as the incident energy increases to keV ranges, the maximum escape yields shift toward incident angle of 30–60°. When the ions with larger incident energies impact the atmosphere, they can penetrate deeper into the lower exobase region and produce more cascade neutrals in the denser atmospheres. Since the trajectories of the glancing ions reside at higher altitudes for a longer time, the cascade collisions occur in the more tenuous atmosphere than those with smaller incident angles. Thus, as the cascade process becomes the dominant producer of hot neutrals, the maximum escape yields move toward smaller incident angles. The sputtered hot corona densities also exhibit similar behaviors as Figure A1.

The digital form of the sputtering tables for the escape yields and the hot corona density at 1000 km can be found at the website: http://sprg.ssl.berkeley.edu/~jinnee.ycwang/SputteringTable/. The density is also fit with the same method as described in sections 3 and 4 with equations (3) and (4). One can use the tables to estimate the sputtering efficiencies when incident pickup O^+ spectra are available from the spacecraft measurements or other simulations results. Cross-checking observations with the estimations from the sputtering response relations can provide better constraint on the sputtering process.

Acknowledgments
We are grateful to NASA's Planetary Science Division for support for this research under grant NNX11AI86G from the MDAP program. The work of X. Fang was supported by NSF grant AST-0908472 and NASA grant NNX11AN38G. Data supporting Figure A1 are available at http://sprg.ssl.berkeley.edu/~jinnee.ycwang/SputteringTable/.

References

Acuña, M. H., et al. (1998), Magnetic field and plasma observations at Mars: Initial results of the Mars global surveyor mission, *Science*, *279*, 1676–1680.
Arkani-Hamed, J. (2001), A 50-degree spherical harmonic model of the magnetic field of Mars, *J. Geophys. Res.*, *106*(E10), 23,197–23,208.
Bird, G. A. (1994), *Molecular Gas Dynamics and the Direct Simulation of Gas Flows*, Clarendon, Oxford, England.
Brain, D., et al. (2010), A comparison of global models for the solar wind interaction with Mars, *Icarus*, *206*, 139–151.
Carr, M. H. (1999), Retention of an atmosphere on early Mars, *J. Geophys. Res.*, *104*, 21,897–21,909.
Chassefière, E., and F. Leblanc (2004), Mars atmospheric escape and evolution; interaction with the solar wind, *Planet. Space Sci.*, *52*, 1039–1058.
Chaufray, J. Y., R. Modolo, F. Leblanc, G. Chanteur, R. E. Johnson, and J. G. Luhmann (2007), Mars solar wind interaction: Formation of the Martian corona and atmospheric loss to space, *J. Geophys. Res.*, *112*, E09009, doi:10.1029/2007JE002915.
Cravens, T. E., J. U. Kozyra, A. F. Nagy, T. I. Gombosi, and M. Kurtz (1987), Electron impact ionization in the vicinity of comets, *J. Geophys. Res.*, *92*(A7), 7341–7353.
Fang, X., M. W. Liemohn, A. F. Nagy, Y. Ma, D. L. D. Zeeuw, J. U. Kozyra, and T. H. Zurbuchen (2008), Pickup oxygen ion velocity space and spatial distribution around Mars, *J. Geophys. Res.*, *113*, A02210, doi:10.1029/2007JA012736.
Fang, X., M. W. Liemohn, A. F. Nagy, J. G. Luhmann, and Y. Ma (2010), On the effect of the Martian crustal magnetic field on atmospheric erosion, *Icarus*, *206*, 130–138.
Fang, X., S. W. Bougher, R. E. Johnson, J. G. Luhmann, Y. Ma, Y.-C. Wang, and M. W. Liemohn (2013), The importance of pickup oxygen ion precipitation to the Mars upper atmosphere under extreme solar wind conditions, *Geophys. Res. Lett.*, *40*, 1922–1927, doi:10.1002/grl.50415.
Hara, T., K. Seki, Y. Futaana, M. Yamauchi, M. Yagi, Y. Motsumoto, M. Tokumaru, A. Fedorov, and S. Barabash (2011), Heavy-ion flux enhancement in the vicinity of the Martian ionosphere during CIR passage: Mars express ASPERA-3 observations, *J. Geophys. Res.*, *116*, A02309, doi:10.1029/2010JA015778.
Jakosky, B. M., and J. H. Jones (1997), The history of Martian volatiles, *Rev. Geophys.*, *35*, 1–16.
Johnson, R. E., and M. Liu (1998), Sputtering of the atmosphere of Mars: 1. Collisional dissociation of CO_2, *J. Geophys. Res.*, *103*(E2), 3639–3647.
Johnson, R. E., and J. G. Luhmann (1998), Sputter contribution to the atmospheric corona on Mars, *J. Geophys. Res.*, *103*(E2), 3649–3653.
Johnson, R. E., D. Schnellenberger, and M. C. Wong (2000), The sputtering of an oxygen thermosphere by energetic O^+, *J. Geophys. Res.*, *105*(E1), 1659–1670.
Lammer, H., et al. (2013), Outgassing history and escape of the Martian atmosphere and water inventory, *Space Sci. Rev.*, *174*, 113–154.
Leblanc, F., and R. E. Johnson (2001), Sputtering of the Martian atmosphere by solar wind pick-up ions, *Planet. Space Sci.*, *49*, 645–656.
Leblanc, F., and R. E. Johnson (2002), Role of molecular species in pickup ion sputtering of the Martian atmosphere, *J. Geophys. Res.*, *107*(E2), 5-1–5-6, doi:10.1029/2000JE001473.
Leblanc, F., J. G. Luhmann, R. E. Johnson, and E. Chassefiere (2002), Some expected impacts of a solar energetic particle event at Mars, *J. Geophys. Res.*, *107*(A5), SIA 5-1–SIA 5-10, doi:10.1029/2001JA900178.
Li, L., Y. Zhang, Y. Feng, X. Fang, and Y. Ma (2011), Oxygen ion precipitation in the Martian atmosphere and its relation with the crustal magnetic fields, *J. Geophys. Res.*, *116*, A08204, doi:10.1029/2010JA016249.
Luhmann, J. G., and J. U. Kozyra (1991), Dayside pickup oxygen ion precipitation at Venus and Mars: Spatial distributions, energy deposition and consequences, *J. Geophys. Res.*, *96*(A4), 5457–5467.
Luhmann, J. G., R. E. Johnson, and M. H. G. Zhang (1992), Evolutionary impact of sputtering of the Martian atmosphere by O^+ pickup ions, *Geophys. Res. Lett.*, *19*(21), 2151–2154.
Ma, Y., and A. F. Nagy (2007), Ion escape fluxes from Mars, *Geophys. Res. Lett.*, *34*, L08201, doi:10.1029/2006GL029208.
Ma, Y., A. F. Nagy, I. V. Sokolov, and K. C. Hansen (2004), Three-dimensional, multispecies, high spatial resolution MHD studies of the solar wind interaction with Mars, *J. Geophys. Res.*, *109*, A07211, doi:10.1029/2003JA010367.
Wang, Y.-C., J. G. Luhmann, F. Leblanc, X. Fang, R. E. Johnson, Y. Ma, W.-H. Ip, and L. Li (2014), Modeling of the O^+ pickup ion sputtering efficiency dependence on solar wind conditions for the Martian atmosphere, *J. Geophys. Res. Planets*, *119*, 93–108, doi:10.1002/2013JE004413.
Zhang, M. H. G., J. G. Luhmann, S. W. Bougher, and A. F. Nagy (1993), The ancient Oxygen exosphere of Mars: Implications for atmosphere evolution, *J. Geophys. Res.*, *98*(E6), 10,915–10,923.
Zuber, M. T., et al. (2000), Internal structure and early thermal evolution of Mars from Mars global survey, topography and gravity, *Science*, *287*, 1788–1792.